Enhanced photocatalytic performance over $Bi_4Ti_3O_{12}$ nanosheets with controllable size and exposed {0 0 1} facets for Rhodamine B degradation

Zhiwu Chen [a,*], Hong Jiang [a], Wuliang Jin [a], Chunkai Shi [b,**]

[a] College of Materials Science and Engineering, South China University of Technology, Guangzhou 510640, China
[b] Department of Chemistry, New Mexico Tech, Socorro, NM 87801, USA

ARTICLE INFO

ABSTRACT

Single-crystalline $Bi_4Ti_3O_{12}$ nanosheets with rectangular shape and exposed {0 0 1} facets were successfully synthesized via a sol–gel hydrothermal process for the first time. Their average side lengths were around 100 and 150 nm, respectively, and thickness ∼20 nm. As a result, the $Bi_4Ti_3O_{12}$ nanosheets reached as high as 79.2% of photodegradation efficiency of Rhodamine B (6 ppm of initial contentration) under 90 min of sunlight irradiation, which was ∼3 times that of conventionally calcined $Bi_4Ti_3O_{12}$. The synthesized nanosheet catalyst also exhibited high reusability for the photodegradation reaction due to the chemical stability of its single crystalline structure. Moreover, photodegradation efficiency of the $Bi_4Ti_3O_{12}$ nanosheets increased as decreasing Rhodamine B concentrations in the range of 6–20 ppm or pH values in the range of 3.1–11.2. Addition of 0.1 M SO_4^{2-} to reaction solution increased almost 6% of photodegradation efficiency of $Bi_4Ti_3O_{12}$ nanosheets under 90 min of illumination. These results demonstrate the superiority of the novel synthetsis technique for preparing bismuth titanate photocatalyst. The much-enhanced photocatalytic performance of $Bi_4Ti_3O_{12}$ nanosheets is attributed to their increased active surface sites, efficient separation and transfer of photogenerated charge carriers and greatly suppressed recombination rate of e^-/h^+ pairs, arising from their large specific surface area, small particle size, single crystallinity, and specific exposed facets.

© 2015 Elsevier B.V. All rights reserved.

1. Introduction

Recently, visible light driven photocatalysis has attracted increasing attention because of its applicability in taking advantage of sunlight to eliminate environmental pollutants [1–4]. TiO_2 is one of the most widely investigated photocatalysts due to its high activity, low cost, and availability. Yet its large band gap (∼3.2 eV) greatly decreases efficient absorption of solar light and restricts practical application in visible light driven catalysis reactions [5]. Chemical modification of TiO_2 is a viable approach to adjust the wide band gap, allowing the active photocatalysts to work in visible light region [6,7].

Bismuth titanate ($Bi_4Ti_3O_{12}$) is a very attractive candidate as highly active photocatalyst due to its unique crystal and electron structures. As a member of Aurivillius family compounds, $Bi_4Ti_3O_{12}$ has a layered perovskite structure built up by $[Bi_2O_2]^{2+}$ fluorite-type and $[Bi_2Ti_3O_{10}]^{2-}$ perovskite-type layers. The $[Bi_2Ti_3O_{10}]^{2-}$ layer is composed of three TiO_6 octahedral layers with Bi^{3+} at an A-site, which are sandwiched between the $[Bi_2O_2]^{2+}$ layers along c-axis [8,9]. Theoretical first-principle calculation suggests that the band structure of $Bi_4Ti_3O_{12}$ is composed of Ti 3d and Bi 6p orbitals for conduction band and hybridization between O 2p and Bi 6s orbitals for valence band. In addition, interaction between Bi and O atoms, integrating the Bi 6s and 6p states in the valence band and the conduction band, should promote the generation and separation of photoexcited electron–hole pairs and thus, narrow its band gap [10]. Subsequently, several visible light sensitive $Bi_4Ti_3O_{12}$ photocatalysts have been developed. For example, $Bi_4Ti_3O_{12}$ nanofibers [11], particulates [12–14], platelets [15], and films [16] have been reported as visible light driven photocatalysts for either energy development or degradation of organic pollutants.

Performance of photocatalysts strongly relies on their sizes, crystallinities, morphologies, and exposed facets [17–22]. For instance, single phase metal oxides are found to be more stable

* Corresponding author. Fax: +86 20 22236602.
** Corresponding author.
E-mail addresses: chenzw@scut.edu.cn (Z. Chen), chunkaishi@yahoo.com (C. Shi).

and active in visible light driven photocatalysis reactions [17–19]. Pore and small $Bi_4Ti_3O_{12}$ nanofibers exhibit enhanced photodegradation performance of Rhodamine B (RhB) and favorable recycling stability under visible light irradiation [20]. Bae and Ohno reported that synthesized TiO_2 particles with specific exposed crystal faces show higher photocatalytic activity for degradation of acetaldehyde and toluene than commercial TiO_2 particles [23]. $Bi_4Ti_3O_{12}$ platelets with both micro scale size and exposed {0 0 1} facets show higher photodegradation activity of methylene blue than commericial TiO_2 [15]. In addition, N-doped $Na_2Ti_6O_{13}@TiO_2$ core–shell nanobelts with exposed {1 0 1} anatase facets display high stability and enhanced catalytic activity for photodegradation of methylene blue under visible light irradiation [4].

Synthesis methods of chemical materials play a vital role in obtaining desired size, morphology, and surface microstructure of products for potential photocatalytic applications [20–22]. Conventionally, $Bi_4Ti_3O_{12}$ powders are synthesized by solid state reaction of Bi_2O_3 and TiO_2 [12,17], which often results in volatilization of Bi_2O_3 and reduces their compositional homogeneity due to high calcination temperature ($\geq 800\,°C$). Several alternative routes, such as chemical solution decomposition [13], sol–gel reaction [24], electrospinning [20], citrate-gel method [25], coprecipitation processes [26], and polymeric precursor method [27], have been developed to obtain $Bi_4Ti_3O_{12}$ with different nanostructures and sizes. Very recently, $Bi_4Ti_3O_{12}$ nanosheets with controllable size and specific exposed facets are prepared via a molten salt synthesis method [28]. Still, these methods require an additional calcination process at temperature of >400 °C, which is far from low cost and may result in agglomeration, inhomogeneous particle size and Bi composition volatilization of products. Therefore, it is of fundamental significance to explore additional synthetic techniques to prepare highly photocatalytic active $Bi_4Ti_3O_{12}$ under more moderate reaction conditions.

As a novel method to prepare desired oxide powders under mild reaction temperatures, sol–gel hydrothermal technique has combined the advantages of both sol–gel synthesis and hydrothermal processing, e.g., high degree of crystallinity, well-controlled morphology, and narrow particle size distribution for the synthesized products [29]. In this work, the process was adopted as a new route to produce single crystal $Bi_4Ti_3O_{12}$ nanosheets with predominantly abundant exposed {0 0 1} facets under the hydrothermal temperature as low as 160 °C. The process has advantages of simplicity, template and surfactant free, and energy-saving. More importantly, the as-prepared $Bi_4Ti_3O_{12}$ nanosheets exhibit highly visible-light-driven photocatalytic activity and favorable stability.

2. Experimental

2.1. Catalyst preparation

$Bi_4Ti_3O_{12}$ nanosheets were prepared via sol–gel synthesis and subsequent hydrothermal processing. First, according to the composition of $Bi_4Ti_3O_{12}$, solutions A and B were obtained by dissolving 0.02 mol $Bi(NO_3)_3 \cdot 5H_2O$ in 15 ml acetic acid and 0.15 mol $Ti(C_4H_9O)_4$ in 15 ml ethylene glycol monomethylether under stirring at room temperature, respectively. All regents were of analytical grade. Solution B was slowly added into solution A dropwise, and the mixture was vigorously stirred for 2 h, resulting in a homogeneous sol. The sol was stabilized when its concentration was adjusted to 0.1 M by adding 10 ml acetic acid and 10 ml ethylene glycol monomethylether, before being heated to 80 °C for 24 h to produce dry gel. The gel was added to 75 ml of a 3 M NaOH solution to form suspension, followed by pouring into a Teflon-lined stainless steel autoclave (volume of 100 ml) with filling capacity of 80% and being subject to hydrothermal treatment at 160 °C for

16 h unless otherwise stated. Finally, the synthesized product was cooled down, filtered, washed with distilled water, and dried at room temperature. For comparison, $Bi_4Ti_3O_{12}$ powders were also prepared via conventional solid-state reaction between TiO_2 and Bi_2O_3 at 800 °C for 3 h, as reported elsewhere [17].

2.2. Characterization

Crystalline structures of powders were examined using an X-ray diffractometer (XRD, D/Max-3C, Rigaku Co.) with Ni-filtered Cu Kα radiation ($\lambda = 1.5418\,Å$) in θ–2θ scan mode, run at 40 kV and 30 mA. The 2θ range and step scan rate were 13–60° and 0.01 °/s, respectively.

Infrared spectra of samples were collected by a Nicolet-Nexus 670 FTIR spectrometer with the scan range of 450–4000 cm^{-1} at a resolution of 4 cm^{-1}. The sample was prepared by the KBr pellet method, with around 1:50 ratio of sample and KBr.

Morphology of sample was observed by a scanning electron microscopy (SEM, LEO 1530 VP, Leo Ltd.) with accelerating voltage of 20 kV, and its composition was examined using energy dispersive spectroscopy (EDS) attached to the SEM. High resolution transmission electron microscopy (HRTEM) of the synthesized products was carried out on a JEOL-2011 instrument with accelerating voltage of 200 kV. The samples were prepared by dispersing $Bi_4Ti_3O_{12}$ powders in anhydrous ethanol with sonication, and dripping on carbon-coated Cu grids.

Specific surface area of samples was measured using the multipoint Brunauer–Emmett–Teller (BET) method (N_2 desorption) at liquid nitrogen temperature (Quantachrome 1900 Corporate Drive). All samples were degassed at 100 °C for 4 h before measurements.

The chemical states of samples were determined using an X-ray photoelectron spectrometer (XPSAxis uhru DCD, UK) with a monochromatic Mg Kα X-ray source. All binding energies were referenced to the C 1s peak at 284.8 eV of the adventitious surface carbon.

The diffuse reflection spectra of the $Bi_4Ti_3O_{12}$ nanosheets were analyzed using a UV–vis spectrophotometer (Model lambda 35, PerkinElmer) with an integrating sphere in the range of 250–800 nm, and $BaSO_4$ was used as the reference.

Zeta potential values of sample were measured using a Zetaplus meter (Brookhaven Instruments, Holtsville, NJ) in the pH range of 1.0–12.0. The sample was prepared by adding ~3 mg of $Bi_4Ti_3O_{12}$ powder to 50 ml DI water, followed by ultrasonic treatment for 15 min to create a suspension. The pH value of the resulting suspension was adjusted using 0.1 M HCl or NaOH.

Photoluminescence (PL) spectra of sample were recorded using a PerkinElmer LS55 fluorescence spectrometer with the excitation wavelength of 320 nm at room temperature. The sample was pressed into a thin disk and fixed on a quartz cell.

Electrochemical experiments were conducted using a CHI 660 electrochemical workstation (CH Instruments, Inc., Austin, USA) with frequencies between 1×10^{-5} and 100 kHz and a potential of 0.17 V at room temperature. All electrochemical measurements were based on a three-electrode system with a $Bi_4Ti_3O_{12}$ electrode (see below for preparation) as the working electrode, a Ag/AgCl (3 M KCl) electrode as the reference electrode and a platinum wire as the auxiliary electrode. 0.1 M KCl and 0.1 M $K_3[Fe(CN)_6]/K_4[Fe(CN)_6]$ in a 1:1 mixture were used as the detecting electrolyte. A 300 W Xe lamp held at 10 cm from the quartz cell with a 420 nm UV filter was used as the visible-light source. The $Bi_4Ti_3O_{12}$ electrodes were prepared as follow: First, 5 mg of $Bi_4Ti_3O_{12}$ nanosheets were added to 0.5 ml solution containing 0.15 ml of pure ethyl alcohol (CH_3CH_2OH) and 0.35 ml of 5% Nafion DE 520 solution (EW is 1000, DuPont). The mixture was then ultrasonically dispersed for 20 min. Finally, 0.1 ml of the well-dispersed $Bi_4Ti_3O_{12}$ slurry were cast onto
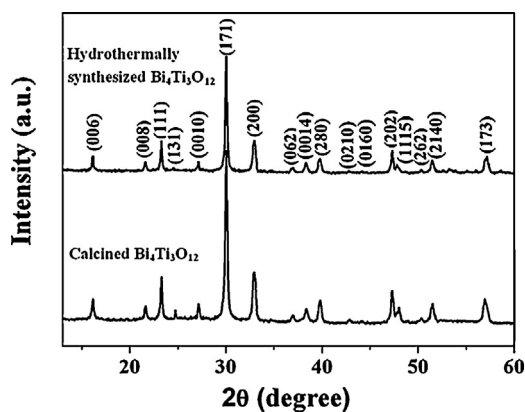
Fig. 1. XRD patterns of prepared $Bi_4Ti_3O_{12}$ powders.

Fig. 2. FTIR spectra of $Bi_4Ti_3O_{12}$ powders with sol–gel synthesis and subsequent hydrothermal process at 160 °C for 16 h.

cleaned ITO glass substrates (<7 ohm/square) to form uniform film electrodes. The $Bi_4Ti_3O_{12}$ electrodes were finally obtained after sintering at 100 °C for 2 h.

2.3. Photocatalytic activity

Photocatalytic activity of the prepared $Bi_4Ti_3O_{12}$ powders was investigated in the decomposition of RhB, a typical organic contaminant, using sunlight illumination. First, 80 mg of $Bi_4Ti_3O_{12}$ powders was added to 80 ml of a 6 ppm RhB aqueous solution (7.1 of pH) in closed cylindrical Pyrex bottles (volume of 100 ml). The whole set up was then placed under sunlight between 12.00 p.m. and 2.00 p.m. in August 2014. The ambient temperature was between 30 and 34 °C. The average insolation of the natural solar light irradiation was 30.43 W/m^2, as measured by a UV irradiance meter in the wavelength range of 375–475 nm. Before irradiation, the suspension was stirred for 45 min and kept in the dark to ensure an adsorption–desorption equilibrium between the photocatalyst and RhB. During irradiation, a 5 ml sample was taken every 15 min, and then centrifuged to separate the spent photocatalyst. The concentration of RhB was analyzed by measuring the absorption intensity at its maximum absorbance wavelength of $\lambda = 553$ nm on a UV–vis spectrophotometer (Model lambda 35, PerkinElmer) with a spectrometric quartz cell of 1 cm path length, and was calculated from a calibration curve. The photodegradation efficiency (PE) of RhB was evaluated by recording the intensity of absorption peak of RhB after the specific irradiation time relative to its initial intensity. For resuability tests, the photocatalytic test over the same $Bi_4Ti_3O_{12}$ nanosheets was repeated three times with 6 ppm of initial concentration of RhB for each test. After each run, the catalyst was recycled by a process of centrifugation, filtration, washing by DI water and drying at 100 °C for 3 h. For concentration-dependent activity tests, initial concentration of RhB was 6, 10, 15, and 20 ppm, respectively. In order to test the photocatalytic activity of $Bi_4Ti_3O_{12}$ nanosheets with additional inorganic ion, 40 ml of 0.2 M NaCl, KNO$_3$, and K$_2$SO$_4$ were added to 40 ml of 12 ppm RhB solution in each run, respectively. For activity test at different pH value, 0.1 M HCl or NaOH was used to adjust acidity or basicity of RhB solution to desired pH value.

3. Results and discussion

3.1. Characterization

3.1.1. Structure and crystallinity

Fig. 1 shows the XRD patterns of the prepared $Bi_4Ti_3O_{12}$ powders. All diffraction peaks of sample with hydrothermal treatment at 160 °C for 16 h can be well indexed to the stan-

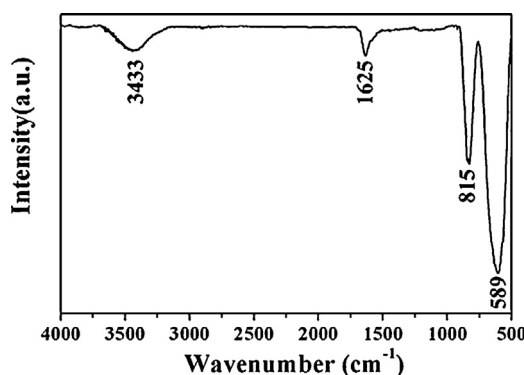dard data of orthorhombic structure of $Bi_4Ti_3O_{12}$ with space group Fmmm and lattice parameters $a = 5.40789$ Å, $b = 5.44678$ Å, $c = 32.83891$ Å (JCPDS 73-2181), indicating that the obtained powders are monophasic bismuth titanate. The sharp diffraction peaks further illustrate the perfect crystallinity of the single-phase $Bi_4Ti_3O_{12}$. The diffraction peaks of the calcined sample were very similar to those of hydrothermally synthesized one, implying they possess very similar crystallized structure. In addition, when hydrothermal temperature was set at 180 °C, the obtained product still had similar diffraction peaks and crystal structure (see Fig. S1 in Supplementary data). However, hydrothermally treated products below 160 °C did not reveal the whole characteristic Bragg peaks for the perfect crystal structure, as also shown in Fig. S1.

FTIR spectra further offer structure information of the hydrothermally treated $Bi_4Ti_3O_{12}$, as shown in Fig. 2. The peaks around 1625 and 3433 cm^{-1} were assigned to the characteristic bending and stretching vibrations of absorbed molecular water, respectively [30]. The others around 815 and 589 cm^{-1} corresponded to the stretching vibrations of Bi—O and Ti—O, respectively, further indicating formation of well crystallized $Bi_4Ti_3O_{12}$ [31,32].

X-ray photoelectron spectroscopy (XPS) was performed to investigate the surface composition and chemical bonding states of the $Bi_4Ti_3O_{12}$ with hydrothermal treatment at 160 °C for 16 h. Based on Fig. 3a, besides weak C 1s peak associated with adventitious hydrocarbon, Bi, Ti, and O core levels were observed. This means that the sample surface mainly consists of Bi, Ti, and O elements. Figs. 3b–d show the high resolution XPS spectra of the Bi 4f, Ti 2p, and O 1s core levels and their Gaussian-resolved results, respectively. The Gaussian-resolved results for Bi 4f spectra in Fig. 3b showed two main peaks centered at 159.56 eV (Bi 4f7/2) and 164.82 eV (Bi 4f5/2), respectively, which are ascribed to Bi^{3+} according to the literature [33]. The two main Gaussian-resolved peaks at 457.62 and 465.49 eV in Fig. 3c were symmetrical, which could be ascribed to the Ti 2p$_{3/2}$ and Ti 2p$_{1/2}$ states of Ti^{4+}, respectively, in good agreement with those in the literature [34–36]. It should be pointed out that the Ti 2p$_{1/2}$ peak was broader than that of pure TiO$_2$ reported in the literature [37]. The broadness of the Ti 2p$_{1/2}$ peak consists with the previous reports where chemical modification of TiO$_2$ leads to broadness of Ti^{4+} XPS spectra [36–38]. Moreover, the high-resolution XPS spectrum of O 1s in Fig. 3d was wide and asymmetric, which could be fitted with three Gaussian-resolved peaks. The main peak at 528.9 eV was attributed to the Bi—O bonds, the small peak at 530.1 eV was assigned to the Ti—O bonds, and the peak at 532.1 eV could be due to the hydroxyl group [36]. All these observations imply that the surface composition of the sol–gel and hydrothermal synthesized $Bi_4Ti_3O_{12}$ could be a single-phase compound [39], which is consistent with the XRD and FTIR results. These
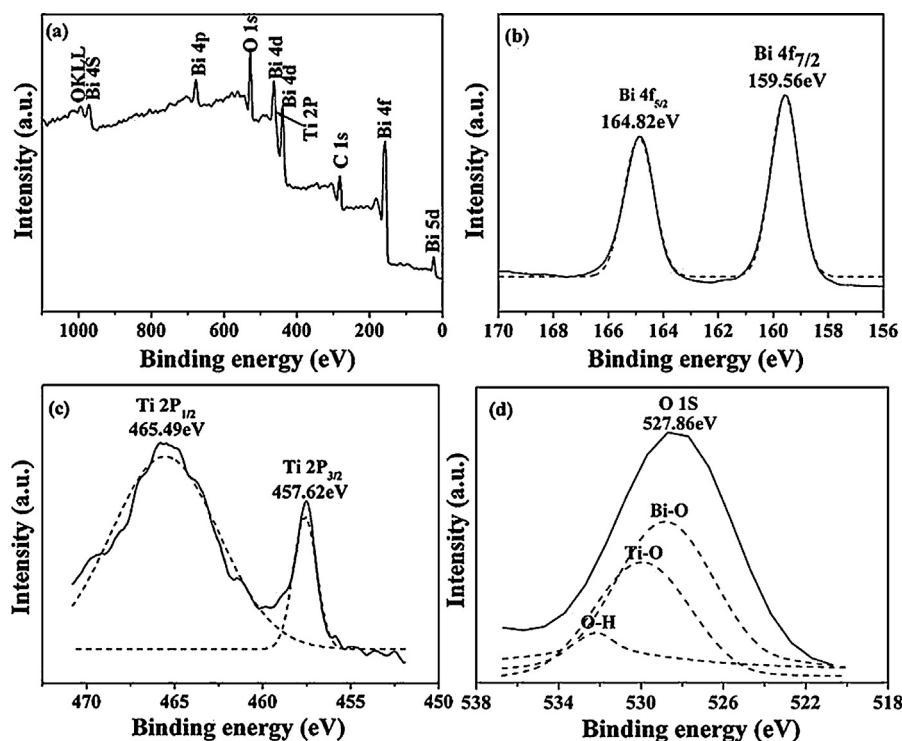
Fig. 3. XPS spectra of the $Bi_4Ti_3O_{12}$ with sol–gel synthesis and subsequent hydrothermal process at 160 °C for 16 h (a) a typical XPS survey spectrum; (b–d) high-resolution XPS core spectra of Bi 4f, Ti 2p, and O1s, respectively.

results confirm the optimum operating temperature is 160 °C for hydrothermally synthesized single-phase $Bi_4Ti_3O_{12}$.

3.1.2. Morphology

Fig. 4a shows SEM micrograph of $Bi_4Ti_3O_{12}$ with hydrothermal treatment at 160 °C. It can be seen that the $Bi_4Ti_3O_{12}$ consisted mostly of regular rectangular nanosheets with narrow distribution of rim size and thin thickness. The nanosheets stacked in disorder, some crossed one another and others paralleled each other, likely due to high surface energy of rectangle shaped nanoparticles. Their average side lengths were 100 and 150 nm, respectively, and thickness ~20 nm. These values are much smaller than those reported recently, where $Bi_4Ti_3O_{12}$-50 nanosheets via molten salt synthesis show the particle size with average side length of 500 nm and thickness of 75 nm [28]. Fig. 4b indicates EDS pattern of the prepared $Bi_4Ti_3O_{12}$ nanosheets. In addition to the observed Cu and C elements from the copper grids made for the SEM samples, three elements of Bi, Ti, and O were evidenced. The ratio of the three elements was estimated and the results were 12.86:9.79:38.69, further demonstrating that the pure $Bi_4Ti_3O_{12}$ was synthesized successfully. Therefore, our observation confirms that controllable size and shape of $Bi_4Ti_3O_{12}$ nanosheet can be easily reached using the sol–gel synthesis and subsequently hydrothermal processing route, which appears to be a better technique to obtain smaller side lengths and thinner thickness of nanosheet than the previously reported molten salt approach [28]. However, when hydrothermal temperature deviated from 160 °C, the obtained products showed either much more irregular morphology of nanosheet or larger particle size than that synthesized at 160 °C (see Fig. S2 in Supplementary data), further identifying the optimum operating temperature of 160 °C.

TEM image of the sample is shown in Fig. 4c. The well-defined nanosheet exhibited a clear rectangular outline with side lengths of around 100 and 150 nm, in line with the SEM results. Fig. 4d reveals HRTEM images of $Bi_4Ti_3O_{12}$ nanosheets. The distinct inter-

planar spacings for the two sets of marked adjacent lattices were 0.271 and 0.273 nm, agreeing well with the (0 2 0) and (2 0 0) planes of $Bi_4Ti_3O_{12}$, respectively [40]. The corresponding selected area electron diffraction (SAED) pattern is displayed in Fig. 4e, confirming that the $Bi_4Ti_3O_{12}$ nanosheets are single crystals. Based on the results described above, the in-plane surfaces of rectangular-shaped nanosheets can be concluded to be (0 0 1) planes, as illustrated in Fig. 4f. For comparison, Fig. 4g shows SEM images of $Bi_4Ti_3O_{12}$ powders calcined at 800 °C. In contrast to the obtained $Bi_4Ti_3O_{12}$ nanosheet, the calcined sample consists of irregularly aggregated particles with sizes of about 0.7–1.5 μm, which is consistent with the previously published work [17]. Therefore, the current sol–gel hydrothermal process not only causes reduction of particle size, but also leads to formation of exposed {0 0 1} facets of $Bi_4Ti_3O_{12}$ nanosheets.

3.2. UV–vis diffuse reflectance spectra

Optical properties of samples were examined using UV–vis diffuse reflection spectrum in the wavelength range of 250–800 nm. As shown in Fig. 5, compared to the calcined sample, $Bi_4Ti_3O_{12}$ nanosheets indicated stronger absorption in the region between λ = 350 and 500 nm. The difference probably results from different crystal growth modes of the two samples. The calcined $Bi_4Ti_3O_{12}$ is formed by the diffusion and counter-diffusion of atoms and/or ionic species between reactants and products, whereas generation of the hydrothermally synthesized one is likely due to a "dissolution–crystallization" mechanism of initially formed nanoclusters [29].

The optical band gap values of samples were calculated using the following equation [20]:

$$\alpha h\nu = A(h\nu - E_g)^{n/2} \tag{1}$$

where A is the absorption coefficient near the absorption edge; h is the Planck's constant with the unit of eV; α is a constant; E_g

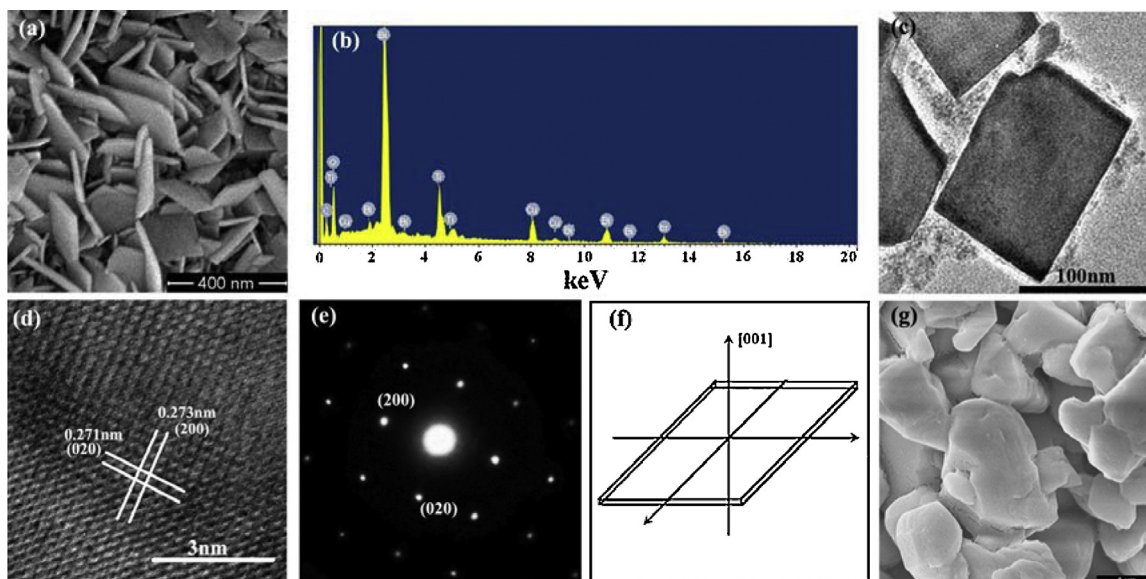**Fig. 4.** (a) SEM image, (b) EDS pattern, (c) TEM, (d) HRTEM, (e) SAED images of $Bi_4Ti_3O_{12}$ powders with sol–gel synthesis and subsequent hydrothermal process at 160 °C for 16 h, (f) schematic illustration of the crystal orientation of the $Bi_4Ti_3O_{12}$ nanosheet, and (g) SEM images of $Bi_4Ti_3O_{12}$ powders synthesized by conventional calcination process at 800 °C for 3 h.
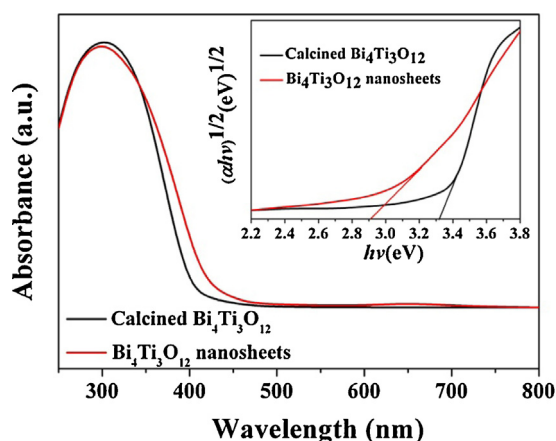

Fig. 5. UV–vis absorption spectrum of the $Bi_4Ti_3O_{12}$ nanosheets and calcined $Bi_4Ti_3O_{12}$ powders. The insert shows the plot of $(\alpha h\nu)^{1/2}$ as a function of photon energy ($h\nu$).

is the absorption band gap energy; and n represents 1 and 4 for direct and indirect band gap semiconductors, respectively [41,42]. $Bi_4Ti_3O_{12}$ had an indirect band gap, and n was 4 herein [10]. The insert of Fig. 5 shows the plot of the $(\alpha h\nu)^{1/2}$ versus $h\nu$, and the values of the band gaps were estimated to be 3.32 eV for the calcined sample and 2.91 eV for $Bi_4Ti_3O_{12}$ nanosheets. The narrower band gap for the latter is probably related to its small particle size and unique morphology [20]. Meanwhile, the lower value implies that the $Bi_4Ti_3O_{12}$ nanosheets could generate more electron–hole pairs under visible-light irradiation than the calcined sample, which would lead to higher photocatalytic performance.

3.3. Photocatalytic performance and reusability

3.3.1. Photocatalytic activity

The photocatalytic activity of samples was investigated by examining degradation of RhB aqueous solution (6 ppm, pH ∼ 7.1) under solar illumination. Fig. 6a shows representative time-dependent absorption spectrum changes of RhB in the presence of

$Bi_4Ti_3O_{12}$ nanosheets. The intensities of the maximum absorption peaks centered at 553 nm dropped rapidly as increasing irradiation time, indicating RhB concentration quickly decreased. Fig. 6b shows its profile of C/C_0 versus reaction time, where C and C_0 are RhB concentrations at a specific irradiation time and the initial time before irradiation, respectively. For comparison, RhB degradation without catalyst or with calcined $Bi_4Ti_3O_{12}$ were also included. The blank tests showed no obvious C/C_0 change in the whole testing period, implying no change in PE, which is expressed as $1 - C/C_0$. The PE value over the calcined $Bi_4Ti_3O_{12}$ was ∼27% during 90 min of illumination. Notably, the $Bi_4Ti_3O_{12}$ nanosheets reached as high as 79.2% of PE in the same illumination time, which was about 3 times that of the calcined $Bi_4Ti_3O_{12}$ and also about 2 times that of product synthesized at 180 °C of hydrothermal temperature (Fig. S3). Fig. 6c displays distinct linear dependence between $\ln(C_0/C)$ and irradiation time, suggesting that the time-dependent photodegradation of RhB follows pseudo-first-order kinetics, i.e., $\ln(C_0/C) = kt$, where t is the irradiation time and k is the rate constant [43]. The calculated rate constant k for $Bi_4Ti_3O_{12}$ nanosheets was 0.0211 min^{-1}, which is around 6 times that of the calcined $Bi_4Ti_3O_{12}$. These findings demonstrate that $Bi_4Ti_3O_{12}$ nanosheets exhibit much better photocatalytic performance as compared to the calcined $Bi_4Ti_3O_{12}$, and also much better than those of $Bi_4Ti_3O_{12}$ nanofibers and Degussa P25 reported in the literature [34,20].

3.3.2. Influences of operating parameters on the photocatalytic performance of $Bi_4Ti_3O_{12}$ nanosheets

3.3.2.1. Influences of RhB concentration.
As shown in Fig. 7, PEs over $Bi_4Ti_3O_{12}$ nanosheets quickly decreased with increasing concentrations of RhB, dropping to ∼53% from 79.2% with change of 6 ppm reactant to 20 ppm. The observation is attributed to significant light adsorption by substrate in the same excitation wavelength range as the photocatalyst. Upon increasing initial RhB concentration, numbers of photon reaching $Bi_4Ti_3O_{12}$ nanosheets decrease because they are increasingly adsorbed by the RhB molecules present both in the solution and on the catalyst surface [44]. Moreover, several layers of adsorbed RhB may be formed on the photocatalyst surface, which is thicker at high RhB concentration and thus, leads to increased distance between the reactants and photocatalyst sur-
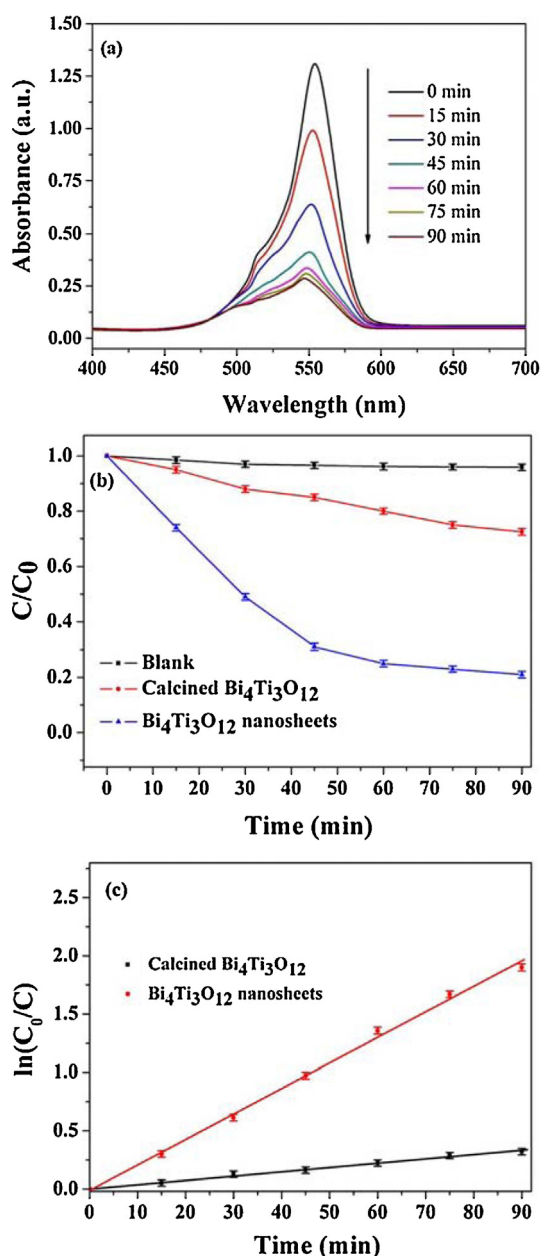
Fig. 7. Influences of RhB concentrations on the photocatalytic activity of $Bi_4Ti_3O_{12}$ nanosheets.

Fig. 8. Influences of electrolytes on the photocatalytic activity of $Bi_4Ti_3O_{12}$ nanosheets ($C_{0,RhB} = 6$ ppm).

Fig. 6. (a) Absorption spectra of Rhodamine B (RhB) under solar light irradiation in the presence of $Bi_4Ti_3O_{12}$ nanosheets ($C_{0,RhB} = 6$ ppm). (b) The photodegradation efficiencies of RhB over $Bi_4Ti_3O_{12}$ samples as a function of irradiation time, and (c) kinetic linear simulation curves of photocatalytic degradation of RhB over $Bi_4Ti_3O_{12}$ nanosheets and calcined $Bi_4Ti_3O_{12}$ powders.

Fig. 9. Influences of pH values on the photocatalytic activity of $Bi_4Ti_3O_{12}$ nanosheets ($C_{0,RhB} = 6$ ppm).

face. As a result, the large amount of the adsorbed RhB inhibits the reaction of reactant molecules with photogenerated holes or hydroxyl radicals.

3.3.2.2. Influences of electrolytes. Fig. 8 shows changes of photodegradation activities in the presence of various inorganic ions, illustrating the effect of Cl^-, NO_3^-, and SO_4^{2-} on photocatalyzed degradation of RhB over $Bi_4Ti_3O_{12}$ nanosheets. Cl^- decreased catalytic activity of $Bi_4Ti_3O_{12}$ nanosheets, showing an inhibitive effect on the photodegradation reaction. As previously reported, Cl^- is regarded as a radical scavenger and could dramatically retard the photocatalytic reaction [45,46]. NO_3^- showed little effect on the photocatalytic reaction, agreeing with results in the literature [47]. Interestingly, SO_4^{2-} apparently promoted the photocatalytic
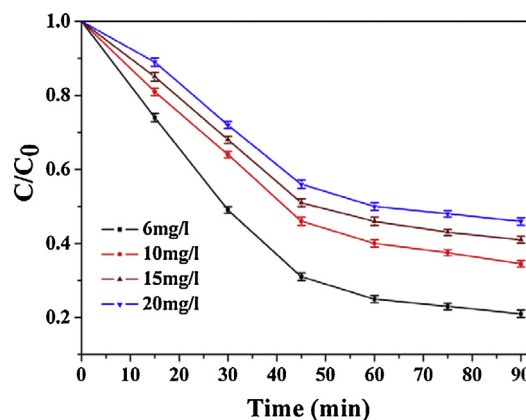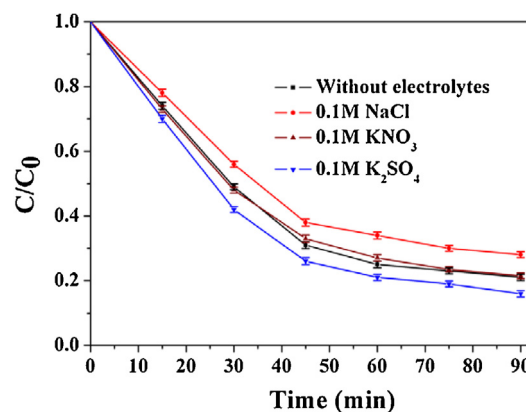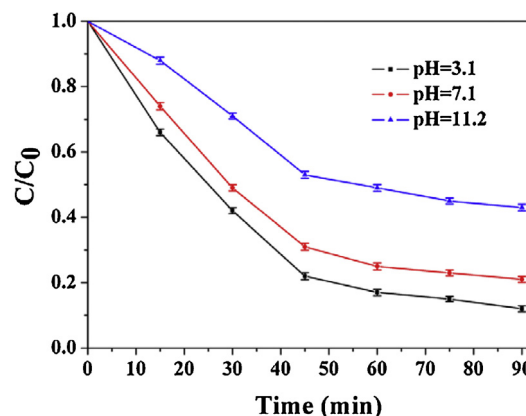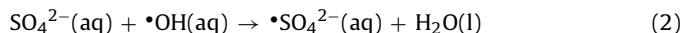
degradation, with PE value increasing by 6% during 90 min of reaction time. The observation could be atributed to reaction of SO_4^{2-} with $^\bullet OH$ to generate $^\bullet SO_4^{2-}$ radical [45,47]:

$$SO_4^{2-}(aq) + {}^\bullet OH(aq) \rightarrow {}^\bullet SO_4^{2-}(aq) + H_2O(l) \qquad (2)$$

As a stronger oxidizing agent, the $^\bullet SO_4^{2-}$ radical could accelerate the photocatalytic reaction.

3.3.2.3. Influences of pH values. Fig. 9 reveals the effect of pH value on the photodegradation activity of $Bi_4Ti_3O_{12}$ nanosheets. The
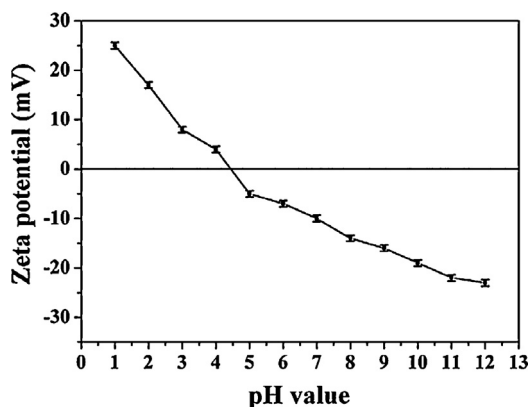
Fig. 10. The zeta potentials of the $Bi_4Ti_3O_{12}$ nanosheeets as a function of pH values.

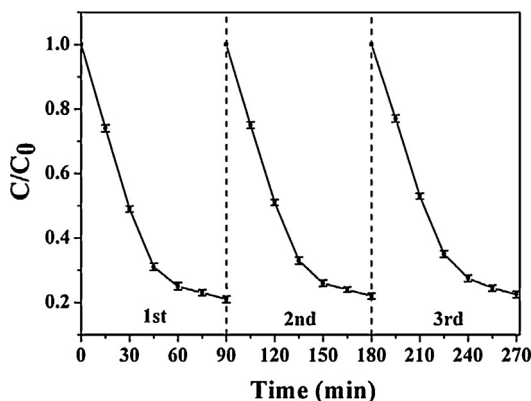**Fig. 12.** XRD patterns of the $Bi_4Ti_3O_{12}$ nanosheets (a) before and (b) after photocatalytic cycling runs.

Fig. 11. Cycling runs of photocatalytic degradation of RhB over $Bi_4Ti_3O_{12}$ nanosheets under sunlight irradiation ($C_{0,RhB} = 6$ ppm).

highest photodegradation activity was observed at pH 3.1. The activity significantly decreased with increasing pH value, with the lowest activity at the highest pH value (11.2). The zeta potential of the $Bi_4Ti_3O_{12}$ nanosheeets as a function of pH values is shown in Fig. 10, with the isoelectric point (IEP) located at a pH of 4.4. The $Bi_4Ti_3O_{12}$ nanosheeets had a high positive charge at pH = 3.1; however, above pH of 7.1, they had a high negative charge. Therefore, at low pH value (3.1), surface coverage of reactant molecules on catalyst could be improved due to electrostatic attraction between positively charged surface of $Bi_4Ti_3O_{12}$ and negatively charged RhB [48,49]. Moreover, $HO_2^{\bullet}$ radicals could form in acid solution, which would compensate for effect of decreasing hydroxyl ions concentration [50]. Also, oxidation could be increased at low pH due to attack of photogenerated hole, which is regarded as the rate determining step in the photocatalytic degradation reaction [49]. These factors contribute to the high photodegradation activity of $Bi_4Ti_3O_{12}$ nanosheets under low pH condition. Conversely, increasing pH (≥ 7.1) of reaction solution would reduce the positive surface charge of $Bi_4Ti_3O_{12}$ nanosheets, and increase electrostatic repulsion between RhB anion and catalyst, which could result in decreased photocatalytic activity [47]. These results indicate that current photodegradation processing of RhB over $Bi_4Ti_3O_{12}$ nanosheet is pH-dependent, consistent with the previous reports [48,50].

3.3.3. Reusability of $Bi_4Ti_3O_{12}$ nanosheets

Fig. 11 shows three cycling runs in the photocatalytic degradation of RhB over $Bi_4Ti_3O_{12}$ nanosheets under solar irradiation ($C_{0,RhB} = 6$ ppm, without electrolytes). At the first cycling run, the PE value was 79.2%, as shown above; after the third cycling run, the

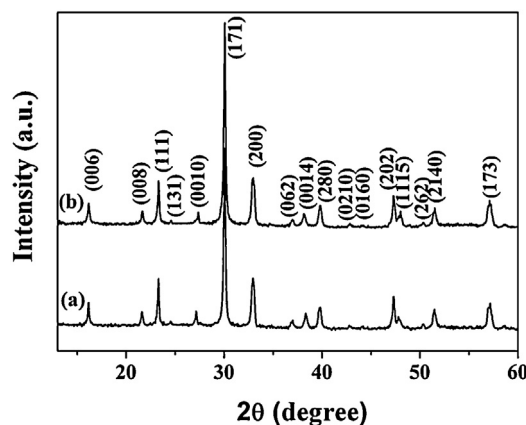PE value was 77.5%, without significant reduction. XRD results of $Bi_4Ti_3O_{12}$ nanosheets before and after three photocatalytic tests showed no observable change of crystalline structure (Fig. 12). All diffraction peaks of fresh and spent catalysts match well with those of the pure orthorhombic $Bi_4Ti_3O_{12}$ (JCPDS No. 73-2181), suggesting that the prepared $Bi_4Ti_3O_{12}$ nanosheets possesses good chemical stability and could be potentially developed as a commercial catalyst.

3.3.4. Origin of enhanced photocatalytic activity over $Bi_4Ti_3O_{12}$ nanosheets

Essentially, catalytic degradation of organic pollution under light illumination condition greatly depends on photoinduced electron–hole pairs, which either directly oxidizes reactant molecules with h^+ or contributes to form active species, such as $^{\bullet}OH$ radicals and super oxide radicals $^{\bullet}O_2^-$ through the oxidation and reduction of the charge carriers [4,14,51,52]. The e^-/h^+ pairs are created along with electron promotion from valence band to conduction band, and most of them recombine in the bulk during their diffusion to reactive surface sites of catalyst. The recombination significantly decreases photodegradation efficiency of catalyst. Therefore, the creation and efficient separation of photoinduced e^-/h^+ pairs play the key role in improving the performance of photocatalyst.

The high specific surface area, crystallinity, and particle size of catalyst substantially influence generation of e^-/h^+ pairs and their efficient separation. These characteristics could explain better photocatalytic performance of $Bi_4Ti_3O_{12}$ nanosheets over the calcined ones for RhB degradation under sunlight.

The particle size and BET specific surface area of photocatalyst have widely been studied in examining possible effects on photodegradation acitivies of organic pollutants because smaller particle size and larger surface area could provide more available active surface sites [53], and decrease in the particle size and increase in the surface area improve quantum efficiency of interfacial charge transfer [54] and are highly preferable for harvesting visible light [1]. The SEM and TEM results confirm the particle size of the synthesized $Bi_4Ti_3O_{12}$ nanosheets was much smaller than that of the calcined one, which would lead to significant change of specific surface area. The BET surface areas were 6.45 $m^2\,g^{-1}$ for the hydrothermally made product and 1.38 $m^2\,g^{-1}$ for the calcined sample. Correspondingly, their apparent reaction rate constances based on the specific surface area can be estimated to be 3.3×10^{-3} and $2.5 \times 10^{-3}\,g\,m^{-2}\,min^{-1}$, respectively. Obviously, the small particle size and the large surface area result in fast reaction rate and thus, improve the photocatalytic activity of $Bi_4Ti_3O_{12}$ nanosheets for the degradation reaction.
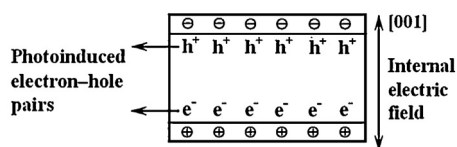
Fig. 13. Proposed mechanism of the photogenerated electron–hole pairs driven apart by the internal electric fields.
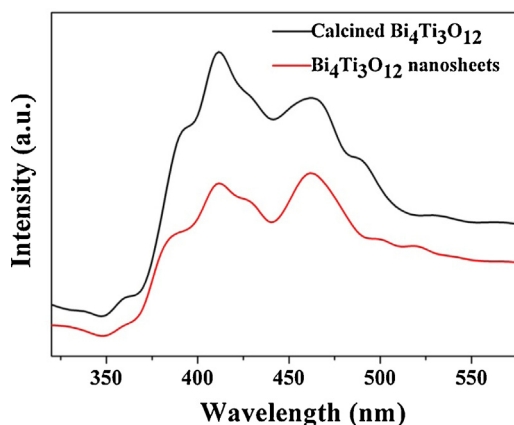

Fig. 14. Photoluminescence (PL) spectra of $Bi_4Ti_3O_{12}$ nanosheets and calcined $Bi_4Ti_3O_{12}$ powders excited at the light wavelength of 320 nm.

The synthesized $Bi_4Ti_3O_{12}$ nanosheets show single crystal structure. It is a layered structure described as the alternate stacking of perovskite slabs $[Bi_2Ti_3O_{10}]^{2-}$ and $[Bi_2O_2]^{2+}$ layers along the pseudotetragonal c-axis [8,9], indicating strongly anisotropic ferroelectric properties. The single crystals exhibit spontaneous polarization (P_s) of $4\,\mu C/cm^2$ along the c-axis [55]. However, a depolarization field would form when the bulk of the ferroelectricity is broken by an interface, such as a nanosheet surface. Correspondingly, internal electric fields are established between the $Bi_4Ti_3O_{12}$ nanosheets, as schematically illustrated in Fig. 13. The self-induced internal electric fields are perpendicular to the nanosheets of $Bi_4Ti_3O_{12}$. The effect of the polarization in ferroelectric materials has proven to be responsible for good photocatalytic activities [56]. When the $Bi_4Ti_3O_{12}$ nanosheets exposed with {0 0 1} facets are irradiated by visible-light, photoinduced electron–hole pairs are formed and then driven apart by the internal electric fields [57]. Consequently, the separation of photogenerated electron–hole pairs along [1 0 0] direction of $Bi_4Ti_3O_{12}$ nanosheets is promoted; the separation of charge carriers by the depolarisation fields also suppresses recombination rate thereby increasing the lifetime of carrier. In addition, small particle size can not only give rise to high specific surface area to offer more active sites, but also decrease traveling path of photoexcited e^-/h^+ pairs within the bulk before reaching the photocatalyst surface [58,59] and thus, contribute to a low recombination rate of charge carriers [60].

Photoluminescence (PL) spectroscopy was applied to evaluate separation efficiency of photogenerated charge carriers in catalysts because recombination of excited electrons and holes generates the PL emission signal [61]. The PL signal intensity is proportional to the recombination rate of photoinduced charge carriers. As shown in Fig. 14, when excited at 320 nm, $Bi_4Ti_3O_{12}$ nanosheets displayed much lower intensities of the emission peaks at around 412 and 461 nm than those of the calcined sample. The decrease of peak intensity suggests that the recombination of photoinduced charge carriers over the $Bi_4Ti_3O_{12}$ nanosheets could be effectively inhibited. Electrochemical impedance spectroscopy was employed to examine the electron-transfer capacity of samples, as shown in Fig. 15. The semicircle part in the Nyquist plots reflects the charge
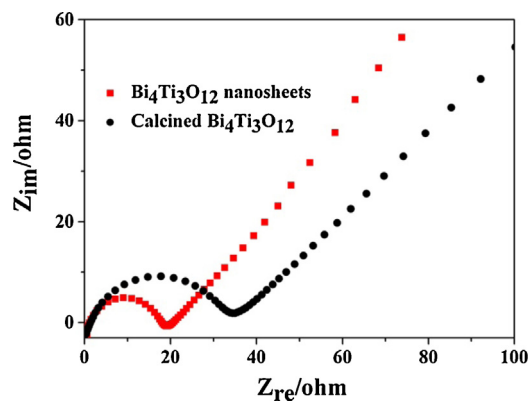

Fig. 15. Nyquist plots for the photoelectrodes of $Bi_4Ti_3O_{12}$ nanosheets and calcined $Bi_4Ti_3O_{12}$ powders in 0.1 M KCl and 0.1 M $K_3[Fe(CN)_6]/K_4[Fe(CN)_6]$ (1:1) solution at pH = 7 under visible-light irradiation ($\lambda > 420$ nm).

transfer process, and the line with a slope of ~45° corresponds to the diffusion-controlled step [62]. The electron-transfer resistance (Rct) was acquired by measuring its diameter, as reported elsewhere [63]. Under visible light irradiation, Rct of the nanosheet electrode was estimated to be around 19 Ω, which is much less than Rct of the electrode made with the calcined sample (34 Ω), suggesting that the hydrothermally synthesized $Bi_4Ti_3O_{12}$ be more efficient for photoinduced charge separation and transfer as compared to the calcined one [62,63].

Based on the above observations, the exposed {0 0 1} facets over hydrothermally synthesized single crystal $Bi_4Ti_3O_{12}$ nanosheets could facilitate the separation and transfer of photogenerated electrons and holes, and thus, greatly suppress recombination of e^-/h^+ pairs, resulting in enhancement in the photodegradation efficiency of RhB. Such benefits have also been observed in the BiOCl single-crystalline nanosheets for photocatalytic degradation of methyl orange [21]. However, the calcined sample had irregular shapes, which is not in favor of charge separation and transfer, leading to much lower photodegradation efficiency than $Bi_4Ti_3O_{12}$ nanosheets. This demonstrates the superiority of the sol–gel hydrothermal method over the conventional solid-state reaction method for preparing highly active $Bi_4Ti_3O_{12}$ photocatalyst.

4. Conclusions

In summary, single-crystalline $Bi_4Ti_3O_{12}$ nanosheets with exposed {0 0 1} facets have been developed via a sol–gel hydrothermal process, which is facile, energy-saving, and surfactant-free. The developed nanosheets possess well-defined rectangular shapes with side lengths of 100–250 nm and thickness of 10–25 nm. Importantly, the obtained nanosheet catalyst exhibits high photodegradation kinetics of RhB, which is around 6 times faster than that of the conventionally calcined sample, which indicates the advantage of the novel synthesis technique for preparing $Bi_4Ti_3O_{12}$ photocatalyst. The much better photodegradation performance of the $Bi_4Ti_3O_{12}$ nanosheet catalyst, as compared with that of the calcined one, is due to its higher specific surface area, unique particle shape, the more active exposed surface and smaller particle size, which offer more active surface sites and are more efficient in delocalizing photoinduced charge carriers and effectively suppress the recombination rate of photogenerated e^-/h^+ pairs. In addition, photocatalytic efficiency of $Bi_4Ti_3O_{12}$ nanosheets increases significantly with decreasing RhB concentration, introducing K_2SO_4 electrolyte or reducing pH value of reaction solution, showing these operating parameters are important factors affecting the photodegradation performance of the catalyst. Finally, a favorable

recycling capability is obtained as well for the $Bi_4Ti_3O_{12}$ nanosheet catalyst, indicating that it could be a promising commercial candidate applied to photocatalytic degradation of organic pollutant under visible light condition.

Acknowledgements

Appendix A. Supplementary data

Supplementary data associated with this article can be found, in the online version, at http://dx.doi.org/10.1016/j.apcatb.2015.07.022

References

[1] X.B. Chen, S. Shen, L. Guo, S. Mao, Chem. Rev. 110 (2010) 6503–6570.
[2] A. Hameeda, M. Aslam, M.I. Iqbal Ismail, S. Chandrasekaran, M.W. Kadi, M.A. Gondal, Appl. Catal. B Environ. 160–161 (2014) 227–239.
[3] S. Dong, J. Feng, Y. Li, L. Hu, M. Liu, Y. Wang, Y. Pi, J. Sun, J. Sun, Appl. Catal. B Environ. 152–153 (2014) 413–424.
[4] C. Liu, T. Sun, L. Wu, J. Liang, Q. Huang, J. Chen, W. Hou, Appl. Catal. B Environ. 170 (2015) 17–24.
[5] X. Hong, Z. Wang, W. Cai, F. Lu, J. Zhang, Y. Yang, N. Ma, Y. Liu, Chem. Mater. 17 (2005) 1548–1552.
[6] N. Wang, L. Zhu, K. Deng, Y. She, Y. Yu, H. Tang, Appl. Catal. B 95 (2010) 400–407.
[7] F. Zuo, K. Bozhilov, R.J. Dillon, L. Wang, P. Smith, X. Zhao, C. Bardeen, P. Feng, Angew. Chem. Int. Ed. 124 (2012) 6327–6330.
[8] B. Park, B. Kang, S. Bu, T. Noh, J. Lee, W. Jo, Nature 401 (1999) 682.
[9] X. Du, I. Chen, J. Am. Ceram. Soc. 81 (1998) 3253.
[10] W. Wei, Y. Dai, B. Huang, J. Phys. Chem. C 113 (2009) 5658.
[11] Y. Liu, M. Zhang, L. Li, X. Zhang, Appl. Catal. B Environ. 160–161 (2014) 757–766.
[12] A. Kudo, S. Hijii, Chem. Lett. 28 (1999) 1103.
[13] W. Yao, H. Wang, X. Xu, S. Shang, Y. Hou, Y. Zhang, M. Wang, Mater. Lett. 57 (2003) 1899.
[14] W. Yao, X. Xu, H. Wang, J. Tao Zhou, X. Yang, Y. Zhang, S. Shang, B. Huang, Appl. Catal. B Environ. 52 (2004) 109–116.
[15] W. Zhao, Z. Jia, E. Lei, L. Wang, Z. Li, Y. Dai, J. Phys. Chem. Solids 74 (2013) 1604–1607.
[16] H. Zhang, M. Lü, S. Liu, L. Wang, Z. Xiu, Y. Zhou, Z. Qiu, A. Zhang, Q. Ma, Mater. Chem. Phys. 114 (2009) 716–721.
[17] W. Zhao, Y. Jin, C. Gao, W. Gu, Z. Jin, Y. Lei, L. Liao, Mater. Chem. Phys. 143 (2014) 952.
[18] H.G. Kim, D. Hwang, J. Lee, J. Am. Chem. Soc. 126 (2004) 8912–8913.
[19] M. Tian, W. Shangguan, J. Yuan, L. Jiang, M. Chen, J. Shi, Z. Ouyang, S. Wang, Appl. Catal. A 309 (2006) 76–84.
[20] D. Hou, W. Luo, Y. Huang, J. Yu, X. Hu, Nanoscale 5 (2013) 2028.
[21] J. Jiang, K. Zhao, X. Xiao, L. Zhang, J. Am. Chem. Soc. 134 (2012) 4473.
[22] X. Han, Q. Kuang, Z. Xie, L. Zheng, J. Am. Chem. Soc. 131 (2009) 3152.
[23] E. Bae, T. Ohno, Appl. Catal. B Environ. 91 (2009) 634–639.
[24] H. Zhang, G. Chen, X. Li, Solid State Ion. 180 (2009) 159.
[25] P. Prakash, A. Garg, M.K. Roy, H.C. Verma, J. Am. Ceram. Soc. 90 (2007) 1295.
[26] N. Pavlovicí, V.V. Srdicí, Mater. Res. Bull. 44 (2009) 860.
[27] B.D. Stojanovic, A.Z. Simoes, C.O. Paiva-Santos, C. Quinelato, E. Longo, J.A. Varela, Ceram. Int. 32 (2006) 707.
[28] H. He, J. Yin, Y. Li, Y. Zhang, H. Qiu, J. Xu, T. Xu, C. Wang, Appl. Catal. B Environ. 156–157 (2014) 35–43.
[29] Y. Hou, L. Hou, S. Huang, T. Zhang, M. Zhu, H. Wang, H. Yan, J. Am. Ceram. Soc. 90 (2007) 1738.
[30] L. Xie, J. Ma, Z. Zhao, H. Tian, J. Zhou, Y. Wang, J. Tao, X. Zhu, Colloid Surf. A 280 (1–3) (2006) 232–236.
[31] H. Gu, P. Chen, Y. Zhou, M. Zhao, A. Kuan, X. Li, Ferroelectrics 211 (1–4) (1998) 271–280.
[32] Y. Kan, X. Jin, G. Zhang, P. Wang, Y. Cheng, D. Yan, J. Mater. Chem. 14 (2004) 3566–3570.
[33] W. Morgan, W. Stec, J. van Wazer, Inorg. Chem. 12 (4) (1973) 953–955.
[34] W. Ren, Z. Ai, F. Jia, L. Zhang, X. Fan, Z. Zou, Appl. Catal. B 69 (3) (2007) 138–144.
[35] J. Hou, R. Cao, Z. Wang, S. Jiao, H. Zhu, J. Mater. Chem. 21 (2011) 7296–7301.
[36] Y. Li, L. Dang, L. Han, P. Li, J. Wang, Z. Li, J. Mol. Catal. A 379 (2013) 146–151.
[37] S. Wang, H. Qian, Y. Hu, W. Dai, Y. Zhong, J. Chen, X. Hu, Dalton Trans. 42 (2013) 1122–1128.
[38] G.S.H. Thien, A. Pandikumar, N.M. Huang, H.N. Lim, Sci. Rep. 4 (2014) 5044.
[39] Y. Wang, L. Zhou, M. Zhang, X. Chen, J. Liu, Z. Liu, Appl. Phys. Lett. 84 (10) (2004) 1731–1733.
[40] J. Dorrian, R. Newnham, M. Kay, D. Smith, Ferroelectrics 3 (1971) 17.
[41] H. Fu, L. Zhang, W. Yao, Y. Zhu, Appl. Catal. B Environ. 66 (2006) 100–110.
[42] H. Jiang, H. Dai, J. Deng, Y. Liu, L. Zhang, K. Ji, Solid State Sci. 17 (2013) 21–27.
[43] V. Stengl, S. Bakardjieva, J. Phys. Chem. C 114 (2010) 19308–19317.
[44] V. Augugliaro, C. Baiocchi, A. Prevot, E. Garcia-Lopez, V. Loddo, S. Malato, G. Marci, L. Palmisano, M. Pazzi, E. Pramauro, Chemosphere 49 (2002) 1223.
[45] M. Abdullah, G.K.C. Low, R.W. Matthews, J. Phys. Chem. 94 (1990) 6820.
[46] I. Arslan, I.A. Balcioglu, D.W. Bahnemann, Appl. Catal. B Environ. 26 (2000) 193.
[47] C. Wang, J. Zhao, X. Wang, B. Mai, G. Sheng, P. Peng, J. Fu, Appl. Catal. B Environ. 39 (2002) 269.
[48] J. Bangun, A.A. Adesina, Appl. Catal. A 175 (1998) 221.
[49] R. Guo, L. Fang, W. Dong, F. Zheng, M. Shen, J. Phys. Chem. C 114 (2010) 21390–21396.
[50] S. Al-Qaradawi, S.R. Salman, J. Photochem. Photobiol. A Chem. 148 (2002) 161.
[51] J.A. Schwarz, C. Contescu, A. Contescu, Chem. Rev. 95 (1995) 477.
[52] Y. Cao, X. Zhang, W. Yang, H. Du, Y. Bai, T. Li, J. Yao, Chem. Mater. 12 (2000) 3445–3448.
[53] M.R. Hoffmann, S.T. Martin, W. Choi, D.W. Bahnemann, Chem. Rev. 95 (1995) 69.
[54] W.G. Becker, M.M. Truong, C.C. Ai, N.N. Hamel, J. Phys. Chem. 93 (1989) 4882.
[55] S.E. Cummins, L.E. Cross, J. Appl. Phys. 39 (1968) 2268.
[56] E. Gutmann, A. Benke, K. Gerth, H. Böttcher, E. Mehner, C. Klein, U. Krause-Buchholz, U. Bergmann, W. Pompe, D.C. Meyer, J. Phys. Chem. C 116 (2012) 5383.
[57] Y. Sun, B.S. Eller, R.J. Nemanich, J. Appl. Phys. 110 (2011), 084303.
[58] S. Li, Y. Lin, B. Zhang, C. Nan, Y. Wang, J. Appl. Phys. 105 (2009), 056105.
[59] Z. Zhang, C. Wang, R. Zakaria, J. Ying, J. Phys. Chem. B 102 (1998) 10871–10878.
[60] K.V. Baiju, A. Zachariah, S. Shukla, S. Biju, M.L.P. Reddy, K.G.K. Warrier, J. Phys. Chem. C 111 (2007) 7612.
[61] J. Tang, Z. Zou, J. Ye, J. Phys. Chem. B 107 (2003) 14265.
[62] R. Pei, Z. Cheng, E. Wang, X. Yang, Biosens. Bioelectron. 16 (2001) 355–361.
[63] J. Hu, Y. Yu, H. Guo, Z. Chen, A. Li, X. Feng, B. Xi, G. Hu, J. Mater. Chem. 21 (2011) 5352.